Time-domain simulation of electron diffraction in crystals

Jia-An Yan
Department of Physics and Astronomy, Vanderbilt University, Nashville, Tennessee 37235, USA
and Department of Physics, Astronomy and Geosciences, Towson University, 8000 York Road, Towson, Maryland 21252

J. A. Driscoll
Department of Physics and Astronomy, Vanderbilt University, Nashville, Tennessee 37235, USA and
College of Engineering and Technology, Bradley University, Peoria, Illinois 61625, USA

B. K. Wyatt and K. Varga
Department of Physics and Astronomy, Vanderbilt University, Nashville, Tennessee 37235, USA

S. T. Pantelides
Department of Physics and Astronomy and Department of Electrical Engineering and Computer Science, Vanderbilt University, Nashville, Tennessee 37221, USA and Oak Ridge National Laboratory, Oak Ridge, Tennessee 37831, USA
(Received 2 August 2011; revised manuscript received 8 December 2011; published 27 December 2011)

Transmission electron microscopy (TEM) and low-energy electron diffraction (LEED) simulations are performed by propagating electron wave packets in real space and real time. The method accurately describes electron scattering in solids for high (>200 keV) and low (20–200 eV) energies. The applicability of the method is demonstrated by calculating TEM images and LEED intensities of silicon and graphene.

DOI: 10.1103/PhysRevB.84.224117 PACS number(s): 73.20.−r, 73.22.−f, 73.50.Bk

I. INTRODUCTION

Electron beams are among the most important tools used to probe the properties of materials at various energy ranges. Low-energy electron diffraction (LEED) is a powerful tool for determining the atomic structure of surfaces.[1–3] In LEED, a collimated electron beam of energy $E = 20$–200 eV (corresponding to a wavelength $\lambda = \sqrt{150/E}$ Å) strikes the surface of a crystalline material. By observing the diffracted electrons as spots on a fluorescent screen, the surface structure can be determined.[4] Low-energy electron point-source microscopy (LEEPS) also utilizes a low-energy electron beam and is important for imaging biological molecules and lensless electron holographic imaging.[5]

On the high-energy side, the electrons used in TEM typically have kinetic energies of $E_k = 100$–300 keV corresponding to a wavelength $\lambda = 0.037$–0.02 Å,[6–8] which enables high-resolution imaging. Unlike the optical microscope, the best achievable spatial resolution in a TEM is not limited by the electron wavelength, but instead is set by the intrinsic imperfections of electron lenses, which are referred to as spherical and chromatic aberrations.[6]

Very recently, the aberration-corrected, monochromated TEAM 0.5 TEM (Ref. 9) has achieved subangstrom resolution[10] for electrons accelerated with an 80-kV voltage.[11–13] The relatively low-energy and aberration-correction technique provide the capability to resolve every single atom in the sample with small radiation damage and high contrast, especially for light element materials.[14] This is important for organic materials, which are too fragile for the high-energy electrons used in other methods. The desired electron energy is from 10 to 100 keV, usually referred to as the intermediate energy range.[6]

Due to the quantum nature of the interaction between electrons and solids, the correct interpretation of the LEED pattern and TEM image requires very careful computer simulations.[2,15–21] For TEM with high-energy electrons, two methods are widely used: the Bloch wave method[22,23] and the multislice theory.[24,25] While the Bloch wave method yields accurate results for crystalline films, it is generally limited to calculations employing relatively small simulation cells. The multislice method, on the other hand, is very successful in describing high-energy TEM imaging. However, due to the approximations adopted in the theory,[21] it may be less accurate in describing the scattering processes for the electrons in the intermediate energy range.

Electron scattering is essentially a time-dependent process. When a free-electron wave packet scatters on the sample, part of the wave packet is reflected back, and the rest is propagated through the solid. Conventional time-independent electron scattering calculations are done in energy space. The wave function in the scattering region is calculated for a given energy and connected to assumed asymptotic states. The calculation has to be repeated for each desired energy. Here, we pursue an alternative approach to calculate the scattering wave function in a time-dependent framework by time propagating a Gaussian wave packet. The time-dependent approach is similar to experiments in that a Gaussian free-electron wave packet is propagated in real time and real space, and the scattering information is extracted from the transmitted and the reflected parts of the wave packet. The main advantage of the approach is that the scattering wave function is calculated for all desired energies at once.

In this work, we present a unified framework to study electron diffraction in solids. We show that both the low- and high-energy electron diffraction patterns can be obtained by propagating the wave packet in real space and real time, and therefore are treated on an equal footing. For high-energy electrons, time-dependent calculations have not been pursued in the past

because the oscillatory nature of the propagated electron wave packet requires an extremely dense grid, which is prohibitively expensive.[21] At these high energies, we use an ansatz in which the incoming electron wave function is expressed by a product of a fast-varying part and a slowly varying envelope function. The slowly varying function will evolve according to a modified Hamiltonian derived from the time-dependent Schrödinger equation. This is somewhat similar to a change in reference frame when analyzing relative object motion. After this transformation, the dense grid sampling becomes unnecessary and electron scattering for both the intermediate- and the high-energy ranges can be described accurately on a regular grid in the time domain. Electron scattering simulations so far have concentrated on static imaging, but the advent of attosecond technology[26] and ultrafast electron microscopy [so called four-dimensional (4D) electron imaging] has made it possible to observe electron dynamics at the sub-fs scale.[27–30] The method presented in this paper could be useful for simulating these ultrafast electron dynamics[31] as well.

II. TIME-DEPENDENT SIMULATION OF ELECTRON SCATTERING

A. Low-energy electrons

With the recent development of ultrafast laser techniques,[26] it has become possible to manipulate electron pulses in a controllable manner.[28,30] The coherence in both space and time can be tuned,[32] which opens up the possibility of studying ultrafast electron dynamics in real space and real time.[30] From a practical applications point of view, as the size of electronic and optoelectronic devices continues to decrease to the nanometer regime, the effect of the electrons' distribution will become relevant for understanding electron dynamics.

The wave-packet (WP) description of an electron is a natural combination of its dual wave and particle nature. As compared to pure plane waves, the wave packet has many advantageous features. The parameters of the Gaussian wave-packet widths can be tuned separately in three directions, allowing for a simulation of the finite-size effects of the electron source.[10] A variety of quantum systems can be controlled with a sequence of short laser pulses, the relative phases of which are finely adjusted to control the interference of electronic or nuclear WPs.[32] Quantum information such as the amplitudes and phases of eigenfunctions superposed to generate a WP can be retrieved. The WP description has been used to study theoretically quantum electron scattering,[33] barrier tunneling,[34–36] and transport.[37] WP propagation in the time domain has been shown to yield the eigenfunctions of arbitrary nanostructures.[38] Very recently, an analogy between the evolution of a free WP and the Fresnel diffraction has been demonstrated.[39] The study of WP dynamics is also of pedagogical interest for visualizing quantum mechanics.[40] Similar to electron scattering, the WP method has also been successfully applied to the study of chemically reactive processes.[41]

We will consider only single electron scattering because the duration ($\sim 10^{-9}$ s) between the electron pulses is much larger than the very fast propagation process ($\sim 10^{-15}$ s) in the solid. We start from the time-dependent Schrödinger equation for the incoming electron wave function $\Phi(r,t)$:

$$i\hbar\frac{\partial\Phi(\mathbf{r},t)}{\partial t} = H\Phi(\mathbf{r},t) = \left[-\frac{\hbar^2}{2m}\nabla^2 + V(\mathbf{r})\right]\Phi(\mathbf{r},t). \quad (1)$$

Here, $V(\mathbf{r})$ is the effective potential of the crystal film, which can be taken as frozen because of the speed of electron propagation.

At $t = 0$, an incoming electron wave packet of initial (average) kinetic energy $E_0 = \hbar^2 k_0^2/2m$ and momentum $p_0 = \hbar k_0$ can be expressed as

$$\Phi(\mathbf{r},t=0) = e^{ik_0 x}\phi_g(\mathbf{r},0), \quad (2)$$

with $\phi_g(\mathbf{r},0)$ the initial distribution of the wave packet. The form of $\phi_g(\mathbf{r},0)$ must be easy to implement in real space, e.g., a Gaussian wave packet (GWP).

The calculation is schematically illustrated in Fig. 1. A wave packet is placed far away from the sample and propagated in time. Part of the wave function is reflected and part of it is transmitted. To avoid artificial reflections from the boundaries of the simulation cell, a complex absorbing potential[42–44] is placed near these boundaries (see Appendix A for further details). Periodic boundary conditions are used in the directions perpendicular to the propagating direction. This boundary condition does not restrict the calculations in any way; the change in interlayer spacing and surface-layer contractions can be included in the calculations.

The wave function is propagated by using

$$\Phi(\mathbf{r},t+\Delta t) = \exp\left(-\frac{iH\Delta t}{\hbar}\right)\Phi(\mathbf{r},t). \quad (3)$$

Once the evolution of the GWP in the whole lattice is complete, we transform the wave function from the time domain into energy space:

$$\Phi(\mathbf{r},E) = \frac{1}{2\pi}\int \Phi(\mathbf{r},t)e^{iEt/\hbar}dt. \quad (4)$$

In the asymptotic regions to the left and right of the sample (see Fig. 1), the wave function can be written a

$$\Phi(\mathbf{r},E) = \begin{cases} e^{i\mathbf{k_{0\parallel}}\cdot\rho}e^{ik_{0\perp}x} + \sum_{\mathbf{g}} R_{\mathbf{k_{0\perp}g}}e^{i(\mathbf{k_{0\parallel}}+\mathbf{g})\cdot\rho}e^{-i\mathbf{k}^-_{g\perp}x}, & x\to-\infty \\ \sum_{\mathbf{g}} T_{\mathbf{k_{0\perp}g}}e^{i(\mathbf{k_{0\parallel}}+\mathbf{g})\cdot\rho}e^{i\mathbf{k}^+_{g\perp}x}, & x\to+\infty \end{cases} \quad (5)$$

where $\rho = (x,y)$. To characterize the scattering for a given energy E, one has to calculate the transmission and reflection coefficients $T_{\mathbf{k_{0\perp}g}}$ and $R_{\mathbf{k_{0\perp}g}}$.

Equation (5) is valid for a thin film where the incident electrons are reflected or transmitted through the sample. In the case of a bulk crystal, there is no transmission and Eq. (5)

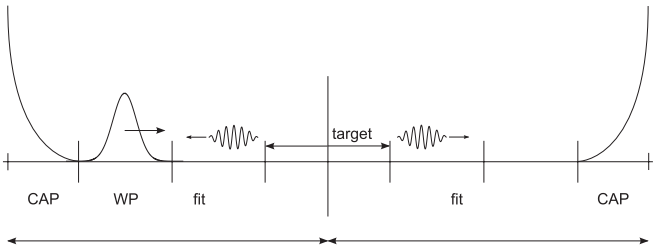

FIG. 1. Schematic illustration of wave-packet propagation.

has to be replaced by

$$\Phi(\mathbf{r},E) = e^{i\mathbf{k_{0\parallel}}\cdot\rho}e^{i\mathbf{k_{0\perp}}x} + \sum_{\mathbf{g}} R_{\mathbf{k_{0\perp}g}}e^{i(\mathbf{k_{0\parallel}}+\mathbf{g})\cdot\rho}e^{-i\mathbf{k}^{-}_{\mathbf{g}\perp}x}, \quad x \to -\infty. \tag{6}$$

In this case, we add a complex absorbing potential (CAP) to the Hamiltonian (see Appendix A for details). The CAP is reflection free, therefore, it does not change the reflection coefficients. The CAP absorbs the electrons deep inside the sample and serves the same purpose as the imaginary potential used in the LEED calculations.[1–3]

The transmission and reflection coefficients in Eqs. (5) and (6) can be determined by fitting the calculated wave function $\Phi(\mathbf{r},E)$ to the asymptotic forms defined in Eq. (5). The details of this calculation are given in Appendix A for one dimension and in Appendix B for three dimensions.

B. Intermediate- and high-energy electrons

For an electron with more than a few tens of keV, a direct calculation of the wave function $\Phi(\mathbf{r},t)$ requires a very dense spatial grid sampling. According to the Nyquist theorem, a small grid spacing $\Delta x < \pi/k_0$ (where $\hbar k_0$ is the electron's momentum) is required in order to account for the rapidly oscillating wave-packet components. This results in the need for a large dense grid (for example, for electrons with 0.02-Å wavelength, the grid spacing should be around 0.002 Å), which is computationally prohibitively expensive.

To avoid this, we note that the electron momentum along the propagation direction (here x) does not change significantly during the scattering process, therefore, the time-dependent wave function can be written as

$$\Phi(\mathbf{r},t) = e^{i(k_0 x - \frac{E_0 t}{\hbar})}\phi_g(\mathbf{r},t), \tag{7}$$

where the electron energy is $E_0 = \hbar^2 k_0^2/2m$. In Eq. (7), the slowly varying and fast-varying parts of the wave function are separated. By substituting Eq. (7) into Eq. (1), we obtain

$$i\hbar\frac{\partial\phi_g(\mathbf{r},t)}{\partial t} = \left[-\frac{\hbar^2}{2m}\nabla^2 + V(\mathbf{r}) - \frac{\hbar^2 k_0}{m}i\frac{\partial}{\partial x} + \mathbf{k}^2\right]\phi_g(\mathbf{r},t) \equiv \mathbf{H}\phi_g(\mathbf{r},t). \tag{8}$$

We can time propagate ϕ_g as

$$\phi_g(\mathbf{r},t) = e^{-\frac{i}{\hbar}\mathbf{H}t}\phi_g(\mathbf{r}-\mathbf{r}_0,0), \tag{9}$$

where the propagator $e^{-\frac{i}{\hbar}\mathbf{H}t}$ can be approximated in many ways, e.g., using a Taylor expansion. The total electron wave function $\Phi(\mathbf{r},t)$ is then given by Eq. (7). Equation (8) is the key equation governing the evolution of the slowly varying part $\phi_g(\mathbf{r},t)$. Since $\phi_g(\mathbf{r},t)$ is slowly varying in space, moderate grid spacings can be used (typically $0.1 \sim 0.3$ Å). By propagating the wave packet according to the modified Hamiltonian $\mathbf{H}$, dense grid sampling can be avoided without loss of accuracy.

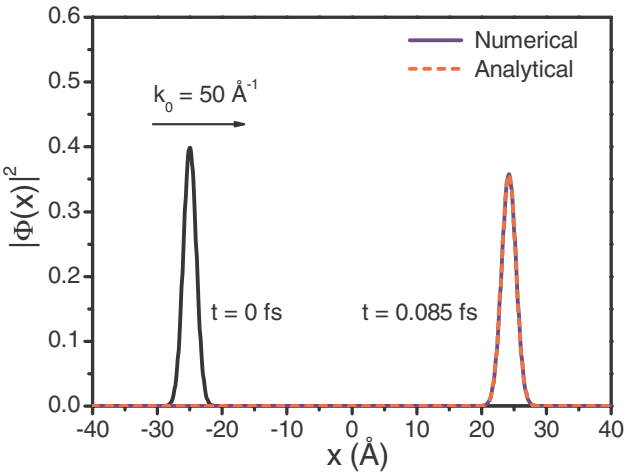

FIG. 2. (Color online) Propagation of a 1D Gaussian wave packet in free space. The wave packet is located at $x = -25$ Åat $t = 0$. Solid line: the wave packet distribution obtained by propagating using Eq. (4). Dashed line: the analytical result. The time step is $\Delta t = 1.0 \times 10^{-5}$ fs. Regular grid spacing $\Delta x = 0.2$ Åis used.

To demonstrate the feasibility of the above technique, we simulate a one-dimensional (1D) GWP propagating in free space, with an initial wave vector of $k_0 = 50$ Å^{-1} ($E_k \sim 10$ keV). Figure 2 shows the wave-packet distribution propagated according to Eq. (8) for $t = 0.085$ fs. The analytical result is also shown for comparison. As can be seen from Fig. 2, the numerical result is in excellent agreement with the analytical solution, demonstrating that the high-energy wave packet can be accurately propagated using Eq. (8).

III. RESULTS AND DISCUSSION

A. Diffraction of low-energy electrons from graphene

As a first example for the application of the time-dependent approach, we show electron diffraction patterns from a graphene sheet. The remarkable properties of graphene have stimulated a large amount of experimental and theoretical research in condensed matter physics and nanoscience.[45,46] One interesting application of graphene is to serve as a support for imaging nanostructures, biomolecules, and soft-hard interfaces.[47,48]

The setup of the computational cell is shown in Fig. 3. We time propagate a single wave packet through the graphene lattice until the scattered wave function is completely adsorbed by the CAP (see Appendix A) at the boundary. The evolution of the wave function with respect to time will be recorded on the two slice planes indicated in Fig. 3. By using Eq. (4), we transform the scattered wave functions from time domain to energy domain, and the diffraction pattern for the energy range of 20 to 200 eV can be obtained in a single calculation.

The reflected electron densities for various incoming electron energies are presented in Figs. 4 and 5, showing the diffraction patterns of graphene. Because the wavelength

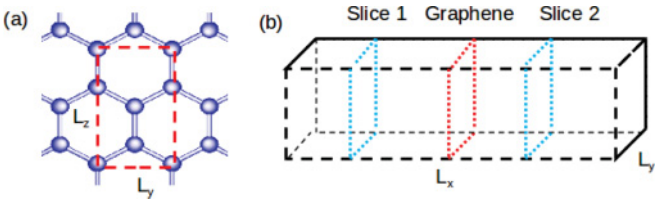

FIG. 3. (Color online) Periodic unit of graphene lattice and our simulation box. $L_x = 60$ Å, $L_y = 2.46$ Å, and $L_z = \sqrt{3}L_y$. The graphene lattice is placed at $L_x = 0$.

of low-energy electrons depends significantly on the energy ($\lambda = \sqrt{150/E}$ Å), the diffraction patterns vary with respect to incoming electron energy.

In Fig. 6, we present the transmission and reflection coefficients calculated by dividing the transmitted and reflected electron intensities through the slice plane by the incoming electron intensity. One can see that within a large energy range (40–200 eV), nearly 80% of the electron beam can penetrate the graphene lattice, showing that the graphene could be useful for LEEPS imaging of biological molecules. A recent LEEPS measurement by Mutus *et al.*[49] showed that nearly 75% of electrons with energy from 100 to 200 eV can penetrate the graphene lattice, in good agreement with our simulation result. From Fig. 6, there is also a considerable portion (around 15%) of the electron beams reflected back from the graphene lattice. This result suggests that graphene could also be useful for in-line reflected holographic imaging.

Our next example is the calculation of the LEED intensity. Two different systems, the diamond(111) 1×1 and the Cu(100) surface, are used as examples. The surface is represented by a few-layer crystal slab. The number of layers is increased until the results converge. In the present case, about 15 atomic layers were found to be satisfactory to obtain accurate results.

The LEED intensity for the diamond surface is shown in Fig. 7. A screened Thomas-Fermi potential is used to represent the carbon atomic potentials. The results of our approach are compared to the intensity curve calculated by the multislice finite difference method[50] (see Fig. 7). The two results are in very good agreement. The slight disagreement is due the use

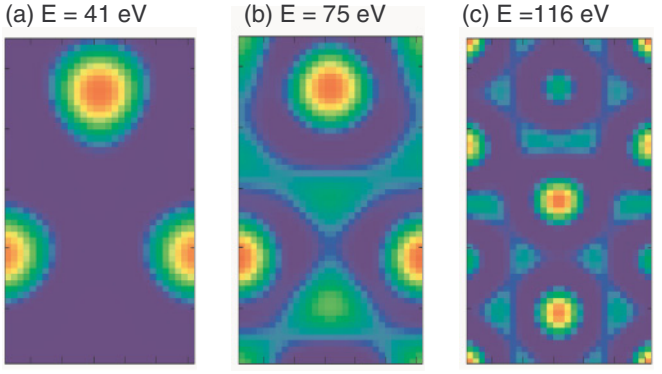

FIG. 4. (Color online) Density distribution for the reflected electron on the slice plane at a distance of 12.0 Å from graphene. (a) $E = 41$ eV, (b) $E = 75$ eV, and (c) $E = 116$ eV.

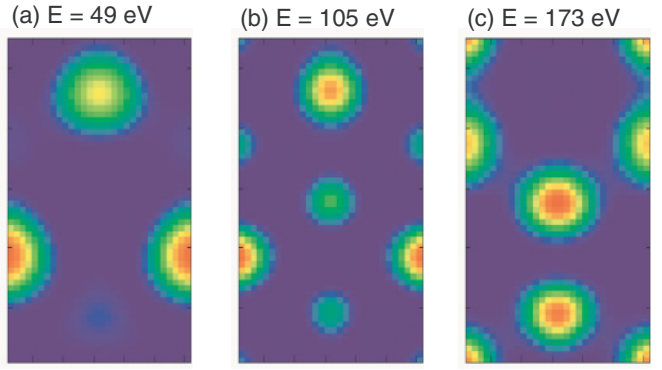

FIG. 5. (Color online) Density distribution for the transmitted electron on the slice plane at a distance of 12.0 Åfrom graphene. (a) $E = 49$ eV, (b) $E = 105$ eV, and (c) $E = 173$ eV.

of different potentials in our calculation (Thomas-Fermi) and in the multislice finite difference approach (muffin-tin).[50]

The calculated LEED intensity for a Cu(100) surface is compared to a tensor LEED calculation[51] in Fig. 8. While the overall agreement between the calculations is good, the differences in the crystal potentials might explain the slight disagreement between the present approach and the tensor LEED results (see Fig. 8). In our approach, the crystal potential was determined by density functional theory (DFT) calculations. In tensor LEED calculations, the crystal potential is modeled by a lattice of muffin-tin potentials characterized by a set of atomic phase shifts and the inelastic processes are modeled by a uniform imaginary potential. The DFT potential is a fully self-consistent potential of the electrons of the crystal. Unlike the muffin-tin potential, the DFT approach properly describes the potential in the interstitial regions, but the inelastic scattering effects are not fully included in the DFT potential. The present approach can use any potential that is numerically or analytically defined in a three-dimensional space grid, including muffin-tin-type potentials, all electron potentials, or pseudopotentials.

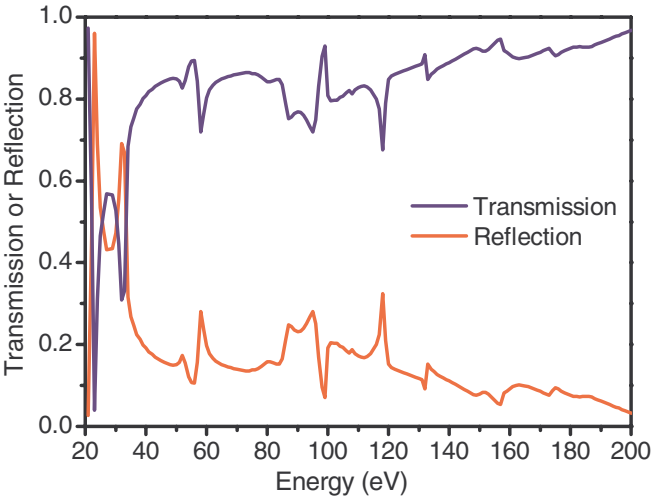

FIG. 6. (Color online) Calculated transmission and reflection coefficients of graphene for the low-energy electron beam.

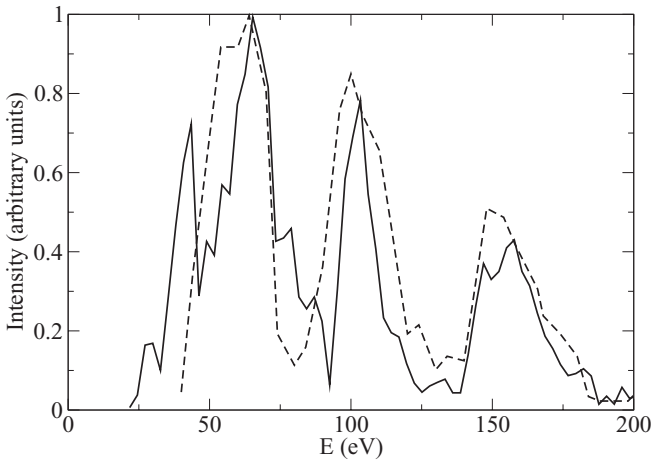

FIG. 7. Intensity curves for a 1 × 1 diamond (111) surface. The solid lines are calculated by the present method and the dashed lines are showing the results of the multislice finite difference approach (Ref. 50). The calculations assumed that normal incidence of the primary electron beam intensity curve belongs to the (00) exit beam.

B. Simulation of transmission electron microscopy (TEM) imaging

The transmission electron microscope (TEM) is a powerful tool for determining crystal structures.[52–56] In high-energy electron microscopy, where the kinetic energy of the incoming electron is much higher than that of the electrons in the film, the crystal potential can be treated as the summation of all atomic potentials in the sample and will not change during the scattering process (i.e., the crystal potential is frozen). Although frozen atomic potentials are used here, a self-consistent all-electron potential calculated by density functional theory can be easily incorporated. In the following, we adopt the all-electron potentials employed in the multislice method, as implemented in Ref. 21.

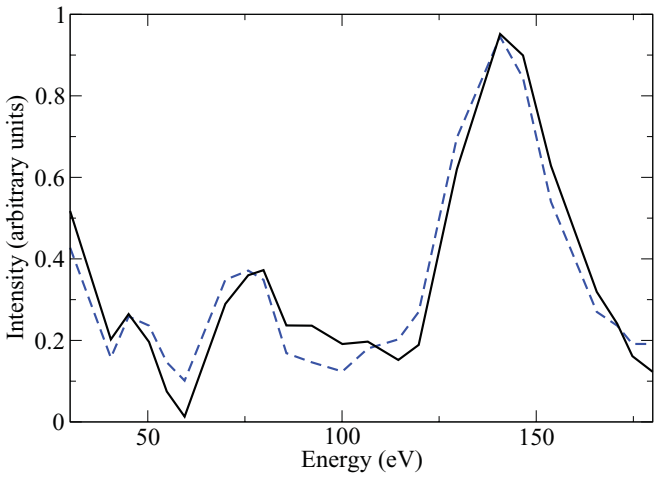

FIG. 8. (Color online) Intensity curves for the Cu(100) surface calculated by the present method (solid line) and by the tensor LEED approach (dashed line). The tensor LEED data are taken from Ref. 51. The calculations assumed that normal incidence of the primary electron beam intensity curve belongs to the (10) exit beam.

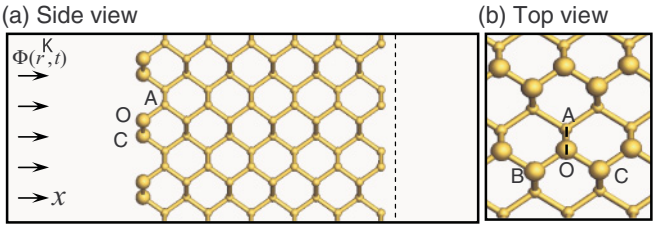

FIG. 9. (Color online) Atomic model for silicon {110} plane used in the simulation: (a) side view and (b) top view. The incoming electron propagates along the x direction (indicated by arrows), perpendicular to the surface. Silicon atoms on the surface (e.g., O and its two nearest-neighbors B and C) are denoted by larger balls, forming a zigzag chain. The center of the coordinates is located at the O atom. One of the nearest neighbors to the silicon atom O inside the film is labeled as A. The position of the exit plane is indicated by a dashed line.

To illustrate the approach, described in Sec. II B, for high-energy electrons, we simulate the TEM image for a silicon thin film along the [110] direction. To obtain the TEM images, a Gaussian wave packet

$$\phi_g(\mathbf{r},0) = \left(\frac{2}{\pi\alpha_0^2}\right)^{\frac{1}{4}} e^{-\frac{(x-x_0)^2}{\alpha_0^2}} \tag{10}$$

is propagated in the x direction as shown in Fig. 9. Periodic boundary conditions are used along the y and z directions. The silicon film (4.4 nm thick) is located at the center of the simulation box. A large vacuum region (more than 10 Å) on both sides of the film along the x direction is used to minimize the possible boundary reflection. For all the simulations below, we fix the grid spacing to be 0.2 × 0.1 × 0.1 Å. Initially, the wave packet center $x = x_0$ is located beyond the region of the crystal potential.

During image formation, the key process is the electron scattering in the crystal film. The exiting scattered wave function will have the necessary information about the crystal structure projected perpendicular to the propagation direction. A direct comparison with the experimental TEM image needs to take into account the instrument's effects, such as the transfer function of the lens. In this work, we focus on the electron scattering in the sample and discuss the scattered wave packet on the exit plane, as indicated by the dashed line in Fig. 9. The projected intensity is calculated by integrating the wave-packet density along the propagating x direction.

Figure 10 shows the results calculated from our time-dependent simulation for a crystalline silicon film at two different energies, 25 and 75 keV. Results from the multislice method as implemented in Ref. 21 are also shown for comparison. The zigzag chain on the projected plane can be identified in all cases. At the 25-keV energy, the intensity distribution obtained from the multislice method in Fig. 10(a) is significantly distorted. In contrast, our time-dependent simulation shows a clear well-known dumbbell structure, as can be seen in Fig. 10(b). At the higher 75-keV energy, the intensity distributions from two methods are similar. This demonstrates that our technique yields accurate results for both the high- and the intermediate-energy ranges.

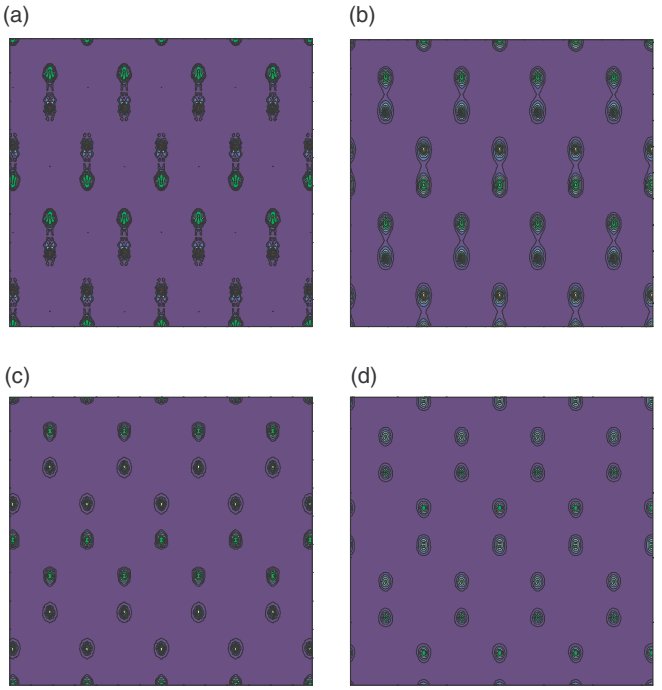

FIG. 10. (Color online) Intensity distribution of the electron wave function at the exit plane obtained from the multislice method and our time-dependent simulation. The thickness of the silicon thin film is 4.4 nm. The incoming electron energies are 25 keV in (a) and (b), and 75 keV in (c) and (d), respectively. (a) and (c): the multislice method; (b) and (d): our time-dependent simulation. The intensity scale of the contour plot is from 1 to 12.

A line scan of the intensity along the projected OA bond allows us to compare the results quantitatively. In Fig. 11, the change of the intensity profiles with respect to the energy are shown. For a fixed thickness, the incoming electron energy varies from 25 to 100 keV. Results from the multislice method are shown as shaded areas.

Comparing the intensities in Figs. 11(a) and 11(b), we find that for a given incoming electron energy, the intensity is smaller for thinner films. Thicker samples give higher contrast. For a given sample thickness, the intensity decreases as the energy increases, which indicates that electrons of lower energy will be scattered more significantly by the crystal potential. This results in a higher intensity contrast. Overall, the results from the two methods are very similar, especially for thin films at intermediate energy ranges and thick samples at high energies. However, as can be seen from the bottom panels in Figs. 11(a) and 10(b), the atomic sites in the profile from the multislice method are not easy to identify. This is also true for the profile of 50 keV in Fig. 11(b). In contrast, our time-dependent simulations yield rather regular intensity profiles for both 25 and 50 keV, as can be seen in Figs. 11(a) and 11(b).

Figure 12 shows the change of intensity with respect to the film thickness for a fixed energy (50 keV). Thicker samples have larger relative intensity signals and therefore higher contrast. Although the two methods give very similar intensity distributions for the thickness of 2.2 nm, a noticeable difference can be seen starting from 4.4 nm, which becomes

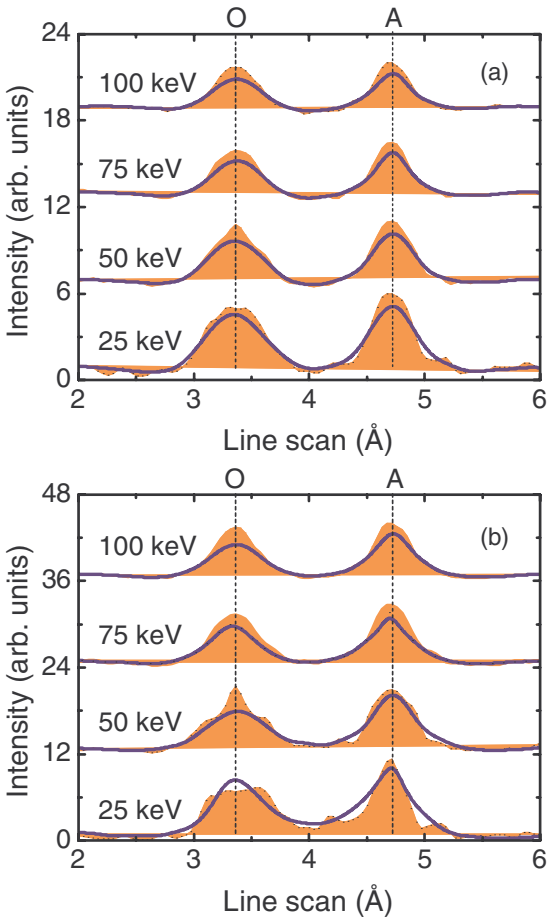

FIG. 11. (Color online) Intensity profile along the projected O–A bond for the silicon thin film with thickness of (a) 2.2 nm and (b) 4.4 nm. The incoming electron energies are 25, 50, 75, and 100 keV, respectively. Blue line: time-dependent simulation; Shaded area: multislice method.

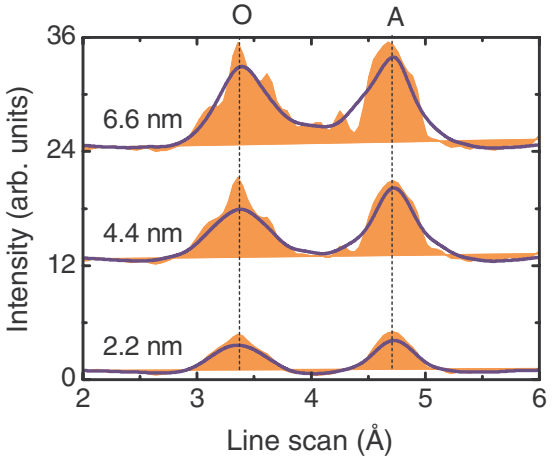

FIG. 12. (Color online) Intensity profile of the projected O–A bond on the *yz* plane for silicon specimen with thickness of 2.2, 4.4, and 6.6 nm. The incoming electron energy is fixed at 50 keV. Blue line: time-dependent simulation. Shaded area: multislice method.

clearer for 6.6 nm. There are several small peaks appearing on the profile from the multislice calculation. The result for 6.6 nm is heavily distorted and the dumbbell structures on the projected plane are barely identified. In contrast, the time-dependent simulation still yields well-defined intensity distributions for thicker samples. Note that in the thick samples, a considerable intensity accumulates between the two atoms, indicating a bonding feature between silicon atoms at O and A sites.

It is well known that the multislice method is more accurate for higher-energy TEM simulation, typically, $E >$ 100 keV. This is because of the approximations employed in the multislice theory, i.e., the second-order term along the propagation direction has been neglected.[21] However, when the energy becomes smaller, the validity of this approximation becomes questionable. As can be seen above, distortions in the intensity distribution become evident for lower-energy electrons and thicker samples, indicating the limitation of the multislice method to the intermediate energy range. In contrast, our time-dependent simulations start from the time-dependent Schrödinger equation. Without any approximation, the time-dependent simulation, in principle, yields the most accurate results for both high- and intermediate-energy ranges. This unified framework might also be useful for the further study of ultrafast electron dynamics in the time domain.

Another advantage of our time-dependent simulation is its ease of use. The multislice method requires a careful choice of the slices along the propagation direction for a given sample. In contrast, only the atomic structure is necessary in our simulations. Therefore, our time-dependent simulation can be easily extended to study more complicated structures, including interfaces and nanostructures.

The present approach is using frozen atomic positions, but the statistical fluctuation of the atomic positions can also be included by averaging the atomic potentials over positions describing the motion of atoms. One way to achieve this is to use the frozen phonon approximation[21] in the same way as in the multislice approach.

IV. SUMMARY

In summary, we have presented a unified framework for simulating electron diffraction in solids in any energy range in real space and real time. The method is straightforward and easy to implement. Since we directly propagate the incoming electron wave function according to the time-dependent Schrödinger equation, the results are expected to be more accurate than previously used methods that are based on various levels of approximations. The main advantage of the method is that the scattering information can be extracted for all energies at once from a single wave-packet propagation, i.e., the calculation does not have to be repeated for many energy points. At the same time, the present method has to be repeated for each scattering direction, while other methods used in LEED calculations can handle all scattering directions at once. The computational time, therefore, depends on the number of required energy points and scattering directions.

Nearly all previous LEED calculations have been performed by employing an average potential, using a muffin-tin shape. Our approach can be implemented with a full potential (e.g., all electron density functional potential) description without relying on a muffin-tin description. In muffin-tin approaches, the potential is averaged around the ionic core with a chosen radius and assumed constant in the interstitial region. This drastic approximation works relatively well in metals, but the agreement with experiments is poorer for materials with covalent bonds.[57] Full potential calculations have been proposed,[50] but their applications so far are limited due to the high computational cost. The present approach greatly reduces the required computational time; most calculations require about an hour on a single processor.

In this work, we have presented examples for the application of the time-dependent approach to low- and high-energy regions. In the intermediate-energy range (10–50 keV), the reflection high-energy electron diffraction (RHEED) technique is used to characterize the surface of crystalline materials. The most accurate method for calculating RHEED intensities was developed by Zhao *et al.*[58] In principle, the present time-dependent approach may also be used to calculate RHEED intensities, and we will implement and test such an approach in the near future.

Using a special ansatz, the rapidly oscillating high-energy scattering wave function can also be simulated by the present approach. The present work is concentrated on time-independent TEM images, but the approach can also be extended to 4D electron imaging to observe electron dynamics at the fs scale.[27–30]

ACKNOWLEDGMENTS

We thank M. Oxley, A. Lupini, and E. Kirkland for useful discussions of multislice simulations. This work was supported in part by DOE Grant No. DE-FG02-09ER46554 and NSF Grant No. CMMI0927345. This research used resources of the National Energy Research Scientific Computing Center, which is supported by the Office of Science of the US Department of Energy under Contract No. DE-AC02-05CH11231.

APPENDIX A: SCATTERING OF LOW-ENERGY ELECTRONS IN 1D

In this Appendix, we show the application of the method to calculate the transmission probability for a one-dimensional finite-square potential barrier. In one dimension, the time-dependent Schrödinger equation reads as

$$i\hbar\frac{\partial\Phi(x,t)}{\partial t} = H\Phi(x,t) = \left[-\frac{\hbar^2}{2m}\nabla^2 + V(x,t)\right]\Phi(x,t). \tag{A1}$$

To solve this equation, the wave function and the Hamiltonian are discretized in space and time using finite differences, and the wave function is time propagated:

$$\Phi(x,t+\Delta t) = \exp[-iH(x,t)\Delta t/\hbar]\Phi(x,t), \tag{A2}$$

where the initial wave function is a chosen to be a Gaussian wave packet

$$\Phi(x,0) = \left(\frac{2}{\pi\alpha_0^2}\right)^{\frac{1}{4}} e^{-\frac{(x-x_0)^2}{\alpha_0^2}} \tag{A3}$$

and a fourth-order Taylor expansion will be used to represent the exponential operator.

Due to the finite size of the lattice grid, if the wave packet spreads quickly, any reflected portion of the wave will then interfere with the incident wave, giving rise to a nonphysical interference pattern. This situation imposes limitations on the choice of the input parameters, e.g., x_0 and α_0 in Eq. (A3), which must be chosen so that the wave functions at the boundaries are essentially zero, at least at the beginning $t = t_0$.[40] To avoid unphysical reflections, a complex absorbing potential (CAP) $iW(x)$ (Refs. 42–44) is added to the Hamiltonian

$$H(x,t) = -\frac{\hbar^2}{2m}\nabla^2 + V(x,t) - iW(x). \tag{A4}$$

The CAP approach is widely used in time-dependent quantum mechanical calculations to avoid artificial reflections caused by the use of finite basis sets or grids.[59] These CAPs are located in the asymptotic region and annihilate the outgoing waves, preventing the undesired reflections (see Fig. 1).

Once the evolution of the GWP in the whole lattice is known for the scattering process, we can transform the WP from t to E:

$$\Phi(x,E) = \frac{1}{2\pi}\int \Phi(x,t)e^{iEt/\hbar}dt. \tag{A5}$$

In the asymptotic region, $\Phi(x,E)$ can be written as

$$\Phi(x,E) = \begin{cases} e^{ikx} + Re^{-ikx}, & x \to -\infty \\ Te^{ikx}, & x \to +\infty. \end{cases} \tag{A6}$$

By writing the asymptotic wave function in this form, we have assumed that the wave packet is propagated from left to right, that is, there is no incoming wave from the right. In principle, one can use Eq. (A6) to extract R and T by fitting the calculated wave function and its derivative to the asymptotic expression. In practice, it is found to be more accurate to fit the wave function in an extended region (see Fig. 1) to the asymptotic form.

To test the approach, a wave packet with initial momentum $k_0 = 6.2$ Å and average energy of 146 eV is scattered at a potential barrier (see Fig. 13). The calculated transmission coefficient, shown in Fig. 14, is in excellent agreement with the analytical results, showing that the scattering information over a wide energy range can be extracted from a single wave-packet propagation.

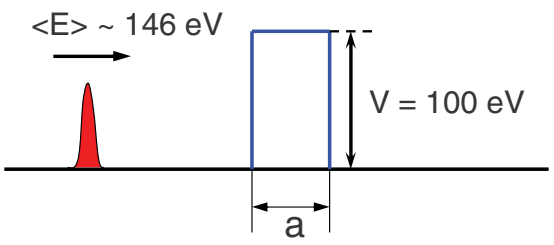

FIG. 13. (Color online) Schematic plot of a Gaussian wave packet tunneling through a square potential barrier. The width of the barrier is $a = 8.3$ Å, and the height of the barrier is $V_0 = 100$ eV. Regular grid spacing of 0.2 Å is used.

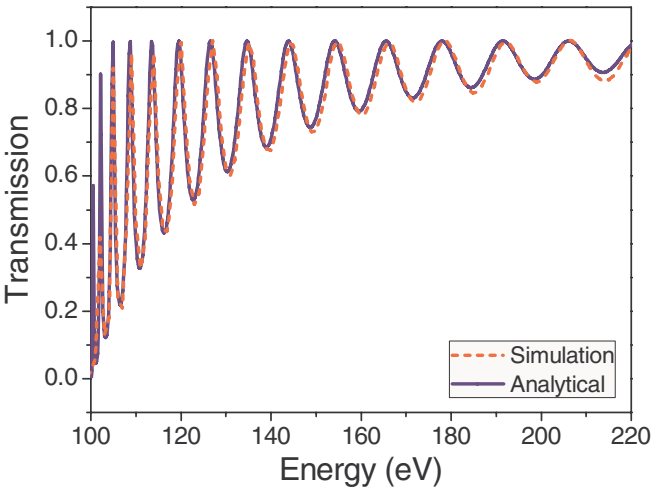

FIG. 14. (Color online) Calculated (solid line) and analytical transmission probability $T(E)$.

As has been discussed in Sec. II A, in case of a bulk target, the asymptotic behavior of $\Phi(x,E)$ can be written as

$$\Phi(x,E) = e^{ikx} + Re^{-ikx}, \quad x \to -\infty, \tag{A7}$$

and a CAP is added to the Hamiltonian to absorb the electrons deep inside the sample. In this work, we will adopt the CAP suggested in Ref. 60. This negative, imaginary CAP is derived from a differential equation and its form is

$$iw(\mathbf{r}) = -i\frac{\hbar^2}{2m}\left(\frac{2\pi}{\Delta x}\right)^2 f(\tilde{x}), \tag{A8}$$

where $\Delta x = x_2 - x_1$, x_1 is the start, and x_2 is the end of the absorbing region, c is a numerical constant, m is the electron's mass, and

$$f(\tilde{x}) = \frac{4}{(c-\tilde{x})^2} + \frac{4}{(c+\tilde{x})^2}, \quad \tilde{x} = \frac{c(x-x_1)}{\Delta x}. \tag{A9}$$

The CAP goes to infinity at the end of the absorbing region and effectively cuts off the bulk beyond that distance.

APPENDIX B: EXTRACTION OF TRANSMISSION AND REFLECTION COEFFICIENTS

In a three-dimensional system, the wave packet can be calculated by time propagation in the same way as in one dimension by extending the grid into three spatial dimensions. The extraction of the scattering information, however, is more complicated because the three-dimensional asymptotic form [Eq. (5)] has to be used.

In the asymptotic region, the wave function can be decomposed into plane waves. One needs to calculate the transmission and reflection probabilities of a plane wave with wave vector $\mathbf{k}_0$ incident on the surface of a slab of crystal. We may decompose $\mathbf{k}_0$ into components parallel and perpendicular to the direction of propagation:

$$\mathbf{k_0} = \mathbf{k_{0\parallel}} + \mathbf{k_{0\perp}}. \tag{B1}$$

When the incident wave reaches the crystal surface, part of the wave function will be reflected. The reflected portion will

travel with wave vectors that can similarly be decomposed into parallel and perpendicular components:

$$\mathbf{k}_{\mathbf{g}}^{-} = \mathbf{k}_{\mathbf{g}\parallel}^{-} + \mathbf{k}_{\mathbf{g}\perp}^{-}. \tag{B2}$$

The other part will be transmitted, with corresponding wave vectors

$$\mathbf{k}_{\mathbf{g}}^{+} = \mathbf{k}_{\mathbf{g}\parallel}^{+} + \mathbf{k}_{\mathbf{g}\perp}^{+}. \tag{B3}$$

Above, we have used + and − to indicate transmission and reflection, respectively. From 2D momentum conservation, we obtain

$$\mathbf{k}_{\mathbf{g}\parallel}^{+-} = \mathbf{k}_{\mathbf{0}\parallel} + \mathbf{g}, \tag{B4}$$

where $\mathbf{g}$ is the 2D reciprocal lattice vector of the crystal. To extract the transmission and reflection coefficients, we proceed by placing matching planes close to the top and bottom of the crystal slab (see Fig. 1). At points above the upper matching plane, we may write the wave function using the incident and reflected plane waves as

$$\Phi(\mathbf{r},E) = e^{i\mathbf{k}_{\mathbf{0}\parallel}\cdot\rho}e^{i\mathbf{k}_{\mathbf{0}\perp}x} + \sum_{\mathbf{g}} R_{\mathbf{k}_{\mathbf{0}\perp}\mathbf{g}}e^{i(\mathbf{k}_{\mathbf{0}\parallel}+\mathbf{g})\cdot\rho}e^{-i\mathbf{k}_{\mathbf{g}\perp}^{-}x}, \tag{B5}$$

where

$$E = \frac{\hbar^2}{2m}(\mathbf{k}_{\mathbf{0}\parallel}{}^2 + \mathbf{k}_{\mathbf{0}\perp}{}^2) \tag{B6}$$

is the electron energy. In the following, in the lower matching plane, we may write the wave function in terms of the transmitted plane waves as

$$\Phi(\mathbf{r},E) = \sum_{\mathbf{g}} T_{\mathbf{k}_{\mathbf{0}\perp}\mathbf{g}}e^{i(\mathbf{k}_{\mathbf{0}\parallel}+\mathbf{g})\cdot\rho}e^{i\mathbf{k}_{\mathbf{g}\perp}^{+}x}. \tag{B7}$$

Once $\Phi(\mathbf{r},E)$ is known, one can use a Fourier transformation over the perpendicular plane (y,z):

$$\sum_{y,z}\Phi(E,\mathbf{r})e^{-i(\mathbf{k}_{0\parallel}+\mathbf{g}')\cdot\rho} = \left[e^{i\mathbf{k}_{\mathbf{0}\perp}x}\delta_{\mathbf{g}',\mathbf{0}} + R_{\mathbf{k}_{\mathbf{0}\perp}\mathbf{g}'}e^{-i\mathbf{k}_{\mathbf{g}'\perp}^{-}x}\right]N_s, \tag{B8}$$

$$\sum_{y,z}\Phi(E,\mathbf{r})e^{-i(\mathbf{k}_{\mathbf{0}\parallel}+\mathbf{g}')\cdot\rho} = T_{\mathbf{k}_{\mathbf{0}\perp}\mathbf{g}'}e^{i\mathbf{k}_{\mathbf{g}'\perp}{}^{+}x}N_s, \tag{B9}$$

where N_s is the number of surface points on our grid. With this transformation, we have obtained an equation that is analogous to Eq. (A6) and the transmission and reflection coefficients can be obtained in a similar way by fitting the Fourier-transformed wave function.

[1] J. B. Pendry, *Low Energy Electron Diffraction* (Academic, New York, 1974).
[2] M. A. Van Hove, W.-H. Weinberg, and C.-M. Chan, *Low-Energy Electron Diffraction* (Springer, Berlin, 1986).
[3] K. Heinz, Rep. Prog. Phys. **58**, 637 (1995).
[4] S. E. Chamberlin, C. J. Hirschmugl, H. C. Poon, and D. K. Saldin, Surf. Sci. **603**, 3367 (2009).
[5] H. J. Kreuzer, K. Nakamura, A. Wierzbicki, H.-W. Fink, and H. Schmid, Ultramicroscopy **45**, 381 (1992).
[6] L. Reimer, *Transmission Electron Microscopy: Physics of Image Formation and Microanalysis* (Springer, Berlin, 1997).
[7] J. C. H. Spence, *Experimental High-Resolution Electron Microscopy,* 3rd ed. (Oxford University Press, New York, 2003).
[8] D. B. Williams and C. B. Carter, *Transmission Electron Microscopy, A Textbook for Materials Science* (Plenum, New York, 1996).
[9] [http://ncem.lbl.gov/TEAM-project].
[10] R. Erni, M. D. Rossell, C. Kisielowski, and U. Dahmen, Phys. Rev. Lett. **102**, 096101 (2009).
[11] J. C. Meyer, C. Kisielowski, R. Erni, M. D. Rossell, M. F. Crommie, and A. Zettl, Nano Lett. **8**, 3582 (2008).
[12] K. W. Urban, Science **321**, 506 (2008).
[13] M. A. O'Keefe, Ultramicroscopy **108**, 196 (2008).
[14] J. C. Meyer, C. O. Girit, M. F. Crommie, and A. Zettl, Nature (London) **454**, 319 (2008).
[15] R. Kilaas, in *Interactive Simulation of High-Resolution Electron Micrographs*, Proceedings of the 45th Annual Meeting of the Microscopy Society of America, edited by G. W. Bailey (San Francisco Press, San Francisco, CA, 1987), pp. 66–69.
[16] R. Kilaas [www.totalresolution.com/index.html].
[17] M. A. O'Keefe and P. R. Buseck, Trans. Am. Crystallogr. Assoc. **15**, 27 (1979).
[18] M. A. O'Keefe and R. Kilaas, in *Image and Signal Processing in Electron Microscopy, Scanning Microscopy*, Supplement 2, edited by P. W. Hawkes, F. P. Ottensmeyer, W. O. Saxton, and A. Rosenfeld (Scanning Microscopy International, Chicago, 1988), pp. 225–244.
[19] J. C. H. Spence and J. M. Zuo, *Electron Microdiffraction* (Plenum, New York, 1992).
[20] P. A. Stadelmann, Ultramicroscopy **21**, 131 (1987); JEMS-EMS Java version, 2004 [cimewww.epfl.ch/people/stadelmann].
[21] E. J. Kirkland, *Advanced Computing in Electron Microscopy* (Plenum, New York, 1998).
[22] H. A. Bethe, Ann. Phys. (NY) **87**, 55 (1928).
[23] M. De Graf, *Introduction to Conventional Transmission Electron Microscopy* (Cambridge University Press, Cambridge, UK, 2003).
[24] J. M. Cowley and A. F. Moodie, Acta Crystallogr. **10**, 609 (1957); **12**, 353 (1959).
[25] P. Goodman and A. F. Moodie, Acta Crystallogr., Sect. A: Cryst. Phys., Diffr. Theor. Gen. Crystallogr. **30**, 280 (1974).
[26] F. Krausz and M. Ivanov, Rev. Mod. Phys. **81**, 163 (2009).
[27] A. H. Zewail, Annu. Rev. Phys. Chem. **57**, 65 (2006).
[28] A. H. Zewail, Science **328**, 187 (2010).
[29] F. Carbone, O.-H. Kwon, and A. H. Zewail, Science **325**, 181 (2009).
[30] P. Baum and A. H. Zewail, Proc. Natl. Acad. Sci. USA **104**, 18409 (2007).
[31] H. Dömer and O. Bostanjoglo, Rev. Sci. Instrum. **74**, 4369 (2003).
[32] K. Ohmori, Annu. Rev. Phys. Chem. **60**, 487 (2009).
[33] B. Ritchie, Phys. Rev. A **45**, R4207 (1992).
[34] J. Wang, Y. Wang, and H. Guo, J. Appl. Phys. **75**, 2724 (1994).

[35]A. P. Stamp and G. C. McIntosh, Am. J. Phys. **64**, 264 (1996).
[36]F. H. Stoica and D. Dragoman, J. Appl. Phys. **86**, 2677 (1999).
[37]S. Monturet and N. Lorente, Phys. Rev. B **78**, 035445 (2008).
[38]D. M. Sullivan and D. S. Citrin, J. Appl. Phys. **91**, 3219 (2002).
[39]T. L. Beach, Am. J. Phys. **77**, 538 (2009).
[40]F. L. Dubeibe, Int. J. Mod. Phys. C **21**, 1391 (2011).
[41]S. C. Althorpe, J. Chem. Phys. **117**, 4623 (2002).
[42]J. G. Muga, J. P. Palao, B. Navarro, and I. L. Egusquiza, Phys. Rep. **395**, 357 (2004).
[43]D. E. Manolopoulos, J. Chem. Phys. **117**, 9552 (2002).
[44]T. Gonzales-Lezena, E. J. Rackham, and D. E. Manolopoulos, J. Chem. Phys. **120**, 2247 (2004).
[45]Y. Zhang, Y.-W. Tan, H. L. Stormer, and P. Kim, Nature (London) **438**, 201 (2005).
[46]K. S. Novoselov, A. K. Geim, S. V. Morozov, D. Jiang, M. I. Katsnelson, I. V. Grigorieva, S. V. Dubonos, and A. A. Firsov, Nature (London) **438**, 197 (2005).
[47]Z. Lee, K.-J. Jeon, A. Dato, R. Erni, T. J. Richardson, M. Frenklach, and V. Radmilovic, Nano Lett. **9**, 3365 (2009).
[48]R. R. Nair, P. Blake, J. R. Blake, R. Zan, S. Anissimova, U. Bangert, A. P. Golovanov, S. V. Morozov, A. K. Geim, K. S. Novoselov, and T. Latychevskaia, Appl. Phys. Lett. **97**, 153102 (2010).
[49]J. Y. Mutus, L. Livadaru, J. T. Robinson, R. Urban, M. H. Salomons, M. Cloutier, and R. A. Wolkow, New. J. Phys. **13**, 063011 (2011).
[50]Huasheng Wu, Jing Wang, Ricky So, and S. Y. Tong, J. Phys.: Condens. Matter **19**, 386203 (2007).
[51]P. J. Rous and J. B. Pendry, Surf. Sci. **219**, 373 (1989).
[52]S. J. Pennycook and L. A. Boatner, Nature (London) **336**, 565 (1988).
[53]N. D. Browning, M. F. Chisholm, and S. J. Pennycook, Nature (London) **366**, 143 (1993).
[54]M. Haider, S. Uhlemann, E. Schwan, H. Rose, B. Kabius, and K. Urban, Nature (London) **392**, 768 (1998).
[55]P. E. Batson, N. Dellby, and O. L. Krivanek, Nature (London) **418**, 617 (2002).
[56]D. A. Muller, Nat. Mater. **8**, 263 (2009).
[57]Edmar A. Soares, Caio M. C. de Castilho, and Vagner E. de Carvalho, J. Phys.: Condens. Matter **23**, 303001 (2011).
[58]T. C. Zhao, H. C. Poon, and S. Y. Tong, Phys. Rev. B **38**, 1172 (1988).
[59]R. Kosloff and D. Kosloff, J. Comput. Phys. **63**, 363 (1986).
[60]D. E. Manolopoulos, J. Chem. Phys. **117**, 9552 (2002).